



Field enhancement and spectral features of hexagonal necklaces of silver nanoparticles for enhanced nonlinear optical processes

ALEJANDRO GÓMEZ-TORNERO,¹ CHRISTOS TSERKEZIS,² JAVIER ROBLEDO MORENO,¹ LUISA E. BAUSÁ,¹ AND MARIOLA O. RAMÍREZ^{1,*}

¹Dpto Física de Materiales, Instituto Nicolás Cabrera and Condensed Matter Physics Center (IFIMAC), Universidad Autónoma de Madrid, 28049 Madrid, Spain

²Center for Nano Optics, University of Southern Denmark, Campusvej 55, DK-5230, Odense M, Denmark

*mariola.ramirez@uam.es

Abstract: The nonlinear properties of hybrid metallic-dielectric systems are attracting great interest due to their potential for the enhancement of frequency conversion processes at nanoscale dimensions. In this work, we theoretically and experimentally address the correlation between the near field distribution of hexagonal plasmonic necklaces of silver nanoparticles formed on the surface of a LiNbO₃ crystal and the second harmonic generation (SHG) produced by this nonlinear crystal in the vicinities of the necklaces. The spectral response of the hexagonal necklaces does not depend on the polarization direction and is characterized by two main modes, the absorptive high-energy mode located in the UV spectral region and the lower energy mode, which is strongly radiant and extends from the visible to the near infrared region. We show that the spatial distribution of the enhanced SHG is consistent with the local field related to the low energy plasmon mode, which spectrally overlaps the fundamental beam. The results are in agreement with the low absorption losses of this mode and the two-photon character of the nonlinear process and provide deeper insight in the connection between the linear and nonlinear optical properties of the hybrid plasmonic-ferroelectric system. The study also highlights the potential of hexagonal necklaces as useful plasmonic platforms for enhanced optical processes at the nanoscale.

© 2018 Optical Society of America under the terms of the [OSA Open Access Publishing Agreement](#)

OCIS codes: (160.2260) Ferroelectrics; (160.4236) Nanomaterials; (160.3730) Lithium niobate; (250.5403) Plasmonics; (190.4350) Nonlinear optics at surfaces; (160.1245) Artificially engineered materials.

References and links

1. M. Kauranen and A. V. Zayats, "Nonlinear plasmonics," *Nat. Photonics* **6**(11), 737–748 (2012).
2. J. Butet, P. F. Brevet, and O. J. F. Martin, "Optical second harmonic generation in plasmonic nanostructures: from fundamental principles to advanced application," *ACS Nano* **9**(11), 10545–10562 (2015).
3. B. Metzger, M. Hentschel, and H. Giessen, "Ultrafast nonlinear plasmonic spectroscopy: from dipole nanoantennas to complex hybrid plasmonic structures," *ACS Photonics* **3**(8), 1336–1350 (2016).
4. A. V. Kachynski, A. Pliss, A. N. Kuzmin, T. Y. Ohulchanskyy, A. Baev, J. Qu, and P. N. Prasad, "Photodynamic therapy by in situ nonlinear photon conversion," *Nat. Photonics* **8**(6), 455–461 (2014).
5. J. Butet, I. Russier-Antoine, C. Jonin, N. Lascoux, E. Benichou, and P. F. Brevet, "Sensing with multipolar second harmonic generation from spherical metallic nanoparticles," *Nano Lett.* **12**(3), 1697–1701 (2012).
6. M. Celebrano, X. Wu, M. Baselli, S. Großmann, P. Biagioni, A. Locatelli, C. De Angelis, G. Cerullo, R. Osellame, B. Hecht, L. Duò, F. Ciccacci, and M. Finazzi, "Mode matching in multiresonant plasmonic nanoantennas for enhanced second harmonic generation," *Nat. Nanotechnol.* **10**(5), 412–417 (2015).
7. D. Smirnova and Y. S. Kivshar, "Multipolar nonlinear nanophotonics," *Optica* **3**(11), 1241–1255 (2016).
8. S.-D. Liu, E. S. P. Leong, G.-C. Li, Y. Hou, J. Deng, J. H. Teng, H. C. Ong, and D. Y. Lei, "Polarization-independent multiple Fano resonances in plasmonic nonamers for multimode-matching enhanced multiband second-harmonic generation," *ACS Nano* **10**(1), 1442–1453 (2016).
9. K. Thyagarajan, J. Butet, and O. J. Martin, "Augmenting second harmonic generation using Fano resonances in plasmonic systems," *Nano Lett.* **13**(4), 1847–1851 (2013).
10. S. Zhang, G. C. Li, Y. Chen, X. Zhu, S. D. Liu, D. Y. Lei, and H. Duan, "Pronounced Fano resonance in single gold split nanodisks with 15 nm split gaps for intensive second harmonic generation," *ACS Nano* **10**(12), 11105–11114 (2016).

11. B. Metzger, L. Gui, J. Fuchs, D. Floess, M. Hentschel, and H. Giessen, "Strong enhancement of second harmonic emission by plasmonic resonances at the second harmonic wavelength," *Nano Lett.* **15**(6), 3917–3922 (2015).
12. K. Y. Yang, J. Butet, C. Yan, G. D. Bernasconi, and O. J. F. Martin, "Enhancement mechanisms of the second harmonic generation from double resonant aluminum nanostructures," *ACS Photonics* **4**(6), 1522–1530 (2017).
13. G. Grinblat, M. Rahmani, E. Cortés, M. Caldarola, D. Comedi, S. A. Maier, and A. V. Bragas, "High-efficiency second harmonic generation from a single hybrid ZnO nanowire/Au plasmonic nano-oligomer," *Nano Lett.* **14**(11), 6660–6665 (2014).
14. J. Richter, A. Steinbrück, M. Zilk, A. Sergeyev, T. Pertsch, A. Tünnermann, and R. Grange, "Core-shell potassium niobate nanowires for enhanced nonlinear optical effects," *Nanoscale* **6**(10), 5200–5207 (2014).
15. H. Linnenbank, Y. Grynko, J. Forstner, and S. Linden, "Second harmonic generation spectroscopy on hybrid plasmonic/dielectric nanoantennas," *Light Sci. Appl.* **5**(1), e16013 (2016).
16. D. Lehr, J. Reinhold, I. Thiele, H. Hartung, K. Dietrich, C. Menzel, T. Pertsch, E. B. Kley, and A. Tünnermann, "Enhancing second harmonic generation in gold nanoring resonators filled with lithium niobate," *Nano Lett.* **15**(2), 1025–1030 (2015).
17. L. Sánchez-García, C. Tserkezis, M. O. Ramírez, P. Molina, J. J. Carvajal, M. Aguiló, F. Díaz, J. Aizpurua, and L. E. Bausá, "Plasmonic enhancement of second harmonic generation from nonlinear RbTiOPO₄ crystals by aggregates of silver nanostructures," *Opt. Express* **24**(8), 8491–8500 (2016).
18. X. Liu, Q. Zhang, W. K. Chong, J. N. Yip, X. Wen, Z. Li, F. Wei, G. Yu, Q. Xiong, and T. C. Sum, "Cooperative enhancement of second-harmonic generation from a single CdS nanobelt-hybrid plasmonic structure," *ACS Nano* **9**(5), 5018–5026 (2015).
19. A. Gómez-Tornero, C. Tserkezis, L. Mateos, L. E. Bausá, and M. O. Ramírez, "2D Arrays of hexagonal plasmonic necklaces for enhanced second harmonic generation," *Adv. Mater.* **29**(15), 160527 (2017).
20. C. Canalias and V. Pasiskevicius, "Mirrorless optical parametric oscillator," *Nat. Photonics* **1**(8), 459–462 (2007).
21. A. Gananni-Padowicz, I. Juwiler, O. Gayer, A. Bahabad, and A. Arie, "All-optical polarization switch in a quadratic nonlinear photonic quasicrystal," *Appl. Phys. Lett.* **94**(9), 091108 (2009).
22. L. Mateos, P. Molina, J. Galisteo, C. López, L. E. Bausá, and M. O. Ramírez, "Simultaneous generation of second to fifth harmonic conical beams in a two dimensional nonlinear photonic crystal," *Opt. Express* **20**(28), 29940–29948 (2012).
23. L. Mateos, M. O. Ramírez, I. Carrasco, P. Molina, J. Galisteo, E. G. Villora, C. de las Heras, K. Shimamura, C. López, and L. E. Bausá, "BaMgF₄: an ultra-transparent two dimensional nonlinear photonic crystal with strong $\chi^{(3)}$ response in the UV spectral region," *Adv. Funct. Mater.* **24**(11), 1509–1518 (2014).
24. M. O. Ramírez, P. Molina, and L. E. Bausá, "Multifunctional solid state lasers based on ferroelectric crystals," *Opt. Mater.* **34**(3), 524–535 (2012).
25. S. V. Kalinin, D. A. Bonnell, T. Alvarez, X. Lei, Z. Hu, J. H. Ferris, Q. Zhang, and S. Dunn, "Atomic polarization and local reactivity on ferroelectric surfaces: a new route toward complex nanostructures," *Nano Lett.* **2**(6), 589–593 (2002).
26. J. N. Hanson, B. J. Rodriguez, R. J. Nemanich, and A. Gruverman, "Fabrication of metallic nanowires on a ferroelectric template via photochemical reaction," *Nanotechnology* **17**(19), 4946–4949 (2006).
27. E. Yraola, P. Molina, J. L. Plaza, M. O. Ramírez, and L. E. Bausá, "Spontaneous emission and nonlinear response enhancement by silver nanoparticles in a Nd³⁺-doped periodically poled LiNbO₃ laser crystal," *Adv. Mater.* **25**(6), 910–915 (2013).
28. L. Mateos, L. E. Bausá, and M. O. Ramírez, "Two dimensional ferroelectric domain patterns in Yb³⁺ optically active LiNbO₃ fabricated by direct electron beam writing," *Appl. Phys. Lett.* **102**(4), 042910 (2013).
29. E. Yraola, L. Sánchez-García, C. Tserkezis, P. Molina, M. O. Ramírez, J. Aizpurua, and L. E. Bausá, "Polarization-selective enhancement of Nd³⁺ photoluminescence assisted by linear chains of silver nanoparticles," *J. Lumin.* **169**, 569–573 (2016).
30. C. Hafner, *Post-modern electromagnetics: using intelligent Maxwell solvers*. (John Wiley & Sons, 1999).
31. H. X. Xu and M. Kall, "Estimating SERS properties of silver-particle aggregates through generalized Mie theory," in *Surface-Enhanced Raman Scattering*. K. Kneipp, M. Moskovits, and H. Kneipp, eds. (Springer-Verlag, 2006).
32. R. L. Chern, X. X. Liu, and C. C. Chang, "Particle plasmons of metal nanospheres: Application of multiple scattering approach," *Phys. Rev. E Stat. Nonlin. Soft Matter Phys.* **76**(1), 016609 (2007).
33. S. J. Barrow, A. M. Funston, D. E. Gómez, T. J. Davis, and P. Mulvaney, "Surface plasmon resonances in strongly coupled gold nanosphere chains from monomer to hexamer," *Nano Lett.* **11**(10), 4180–4187 (2011).
34. C. Tserkezis, R. W. Taylor, J. Beitner, R. Esteban, J. J. Baumberg, and J. Aizpurua, "Optical response of metallic nanoparticle heteroaggregates with subnanometric gaps," *Part. Part. Syst. Charact.* **31**(1), 152–160 (2014).
35. B. Willingham and S. Link, "Energy transport in metal nanoparticle chains via sub-radiant plasmon modes," *Opt. Express* **19**(7), 6450–6461 (2011).
36. L. S. Slaughter, B. A. Willingham, W.-S. Chang, M. H. Chester, N. Ogden, and S. Link, "Toward plasmonic polymers," *Nano Lett.* **12**(8), 3967–3972 (2012).
37. R. Esteban, R. W. Taylor, J. J. Baumberg, and J. Aizpurua, "How chain plasmons govern the optical response in strongly interacting self-assembled metallic clusters of nanoparticles," *Langmuir* **28**(24), 8881–8890 (2012).

38. E. Yraola, L. Sánchez-García, C. Tserkezis, P. Molina, M. O. Ramírez, J. L. Plaza, J. Aizpurua, and L. E. Bausá, "Controlling solid state gain media by deposition of silver nanoparticles: from thermally- quenched to plasmon-enhanced Nd^{3+} luminescence," *Opt. Express* **23**(12), 15670–15679 (2015).
39. G. Aguirregabiria, J. Aizpurua, and R. Esteban, "Self-assembled flat-faceted nanoparticles chains as a highly-tunable platform for plasmon-enhanced spectroscopy in the infrared," *Opt. Express* **25**(12), 13760–13772 (2017).
40. P. Molina, E. Yraola, M. O. Ramírez, C. Tserkezis, J. L. Plaza, J. Aizpurua, J. Bravo-Abad, and L. E. Bausá, "Plasmon-assisted Nd^{3+} -based solid-state nanolaser," *Nano Lett.* **16**(2), 895–899 (2016).
41. D. Hernandez-Pinilla, P. Molina, C. de las Heras, J. Bravo-Abad, L. E. Bausá, and M. O. Ramírez, "Multiline operation from a single plasmon-assisted laser," *ACS Photonics* **5**(2), 406–412 (2018).
42. S. A. Maier, M. L. Brongersma, P. G. Kik, S. Meltzer, A. A. G. Requicha, and H. A. Atwater, "Plasmonics - a route to nanoscale optical devices," *Adv. Mater.* **13**(19), 1501–1505 (2001).
43. D. Solis, Jr., A. Paul, J. Olson, L. S. Slaughter, P. Swanglap, W. S. Chang, and S. Link, "Turning the corner: efficient energy transfer in bent plasmonic Nanoparticle chain waveguides," *Nano Lett.* **13**(10), 4779–4784 (2013).
44. R. Thomas and R. S. Swathi, "Linear and polygonal assemblies of plasmonic nanoparticles: incident light polarization dictates hot spots," *J. Phys. Chem. C* **120**(33), 18733–18740 (2016).

1. Introduction

Over the last few years, the study of plasmon enhanced nonlinear optical processes at the nanoscale has been receiving significant attention due to their potential applications in a diversity of disciplines such as molecular sensing, advanced spectroscopies or integrated photon sources for optical circuits [1–5]. Most of these functionalities rely on the capability of nonlinear frequency converters to operate in a broad spectral range (from the UV down to the mid-infrared spectral region) with a controlled polarization state and high frequency stability. While different designs have been used to exploit frequency conversion phenomena at the nanoscale [6–12], the combination of plasmonic nanostructures with nonlinear dielectric crystals has been scarcely addressed. However, the association of metallic nanostructures supporting plasmonic modes with nonlinear crystals has shown to be a useful route for boosting the nonlinear response at the nanoscale, i.e. at the vicinities of the metallic nanostructures [13–19].

Among the nonlinear dielectric materials, ferroelectric domain structures stand out for their exceptional properties for light generation and control. They have been successfully used in optical parametric processes [20], phase control and all-optical polarization switching [21], or in the development of novel light sources enabling the simultaneous generation of multiple nonlinear processes [22, 23]. Ferroelectric domain patterns can also incorporate optically active rare earth ions during their crystal growth, thus acting as self-frequency conversion solid state lasers [24]. Further, in the last years, opposite-polarity ferroelectric domains structures have been employed as templates on which different type of metallic nanostructures can be assembled on their surface [25–27]. By means of domain selective photo-reduction of silver cations we have shown the formation of plasmonic chains and hexagonal necklaces of silver nanoparticles (NPs) on the domain boundary surfaces of LiNbO_3 . Arrangements composed of 50 nm sized NPs separated a few nanometers can be obtained by a fine control of the photo-deposition conditions. The small inter-particle distances ensure a strong interaction among them, which gives rise to a broad plasmonic resonance covering the UV-near infrared (NIR) spectral range [19, 27]. Indeed, the plasmonic response provided by the hexagonal necklaces of silver NPs was recently exploited to produce up to a 400-fold SHG enhancement in the near UV spectral region [19]. The mechanism responsible for this intensification has been mainly related to the local field enhancement of the fundamental beam, which participates with two photons in the SHG process.

In this work, we evaluate the effect of wavelength and polarization on the near field distribution of the hexagonal necklaces and how these features affect the experimental spatial distribution of the enhanced SH signal generated by the LiNbO_3 crystal at the vicinities of the hexagonal metallic arrangements. On one side, we theoretically analyze the effect of

increasing the number of particles on the far field extinction cross-section spectra of the hexagons and evaluate the spectral convergence as well as the radiative and non-radiative properties of the main collective plasmonic modes. We also study the influence of the incoming polarization and demonstrate that the far field extinction spectrum does not vary with the polarization direction, in agreement with the high symmetry of the hexagonal necklaces. On the other hand, we provide a detailed picture of the near field response of the hexagonal necklaces by analyzing the distribution of field enhancement at different wavelengths and polarization configurations. The relevant near field profiles are then compared with the spatial distribution of the SHG signal, and the role of the plasmon enhanced excitation and/or emission wavelengths on boosting the SHG response is discussed. Our analysis is relevant to determine the configuration of the electromagnetic fields generated by hexagons of nanoparticles and thus, to manipulate and control the optical performance of nonlinear nano-devices. The study constitute a necessary step to take advantage of (or to implement) the optical performance of hexagonal necklaces at the nanoscale and provides deeper insight in the connection between the linear and nonlinear optical properties of the hybrid plasmonic-ferroelectric system.

2. Experimental methods

2.1 Fabrication of hexagonal necklaces of Ag NPs on LiNbO₃ crystal

Ferroelectric domain patterns of hexagonal domains were fabricated in a LiNbO₃ crystal by direct electron beam irradiation using a Philips XL30 SFEG electron microscope driven by Elphy Raith nanolithography software. For the photo-deposition of metallic nanoparticles, the domain patterned ferroelectric crystal was polished up to optical grade and immersed into a 0.01M AgNO₃ solution. After illuminating the sample with above band gap UV radiation during four minutes at 60°C, plasmonic necklaces of Ag NPs were formed on the hexagonal domain boundary surfaces. The average size of the nearly spherical Ag NPs was about 50 nm and the interspacing distance was close to 2 nm.

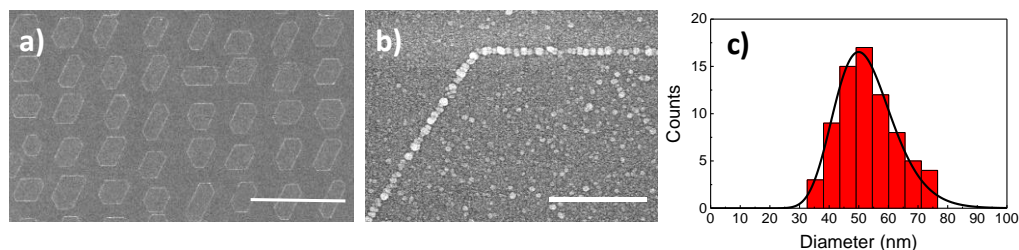


Fig. 1. a) Representative SEM image of a square-like arrangement of hexagonal necklaces of Ag NPs formed on the polar surface of a LiNbO₃ crystal. The scale bar is 10 μm. b) High-resolution SEM image showing a detail of one corner of the hexagonal necklace. The scale bar corresponds to 500 nm. c) Histogram and distribution of the NPs diameter forming the plasmonic necklaces.

Figure 1 shows a representative SEM image of a square-like arrangement of hexagonal necklaces distributed on the polar surface of the LiNbO₃ crystal. A certain elongation of the plasmonic hexagons along the Y crystallographic direction is observed, in agreement with the shapes of the ferroelectric domains, which tend to grow preferably along the Y crystallographic direction. Further details can be found in [19, 28]. To assess the quality of the structure, Fig. 1(b) shows a more detailed view of one corner the hexagons. The size distribution of the NPs forming the hexagonal necklaces is displayed in Fig. 1(c). As observed, the NPs size range from around 35 to 75 nm with a maximum centered at around 50 nm. As previously reported for linear chains of NPs formed on the same substrate, mixing spherical interacting NPs with different sizes results into plasmonic modes with resonances located at intermediate wavelengths values [29]. Therefore, the NPs necklaces can be well

modeled by spheres with a size corresponding to the average size of the distribution, 50 nm in our case.

2.2 Numerical calculations

To simulate the optical response of the hexagonal necklaces we use numerical calculations based on the multiple multipole method (OpenMaXwell, openmax.ethz.ch). This method has shown to be extremely efficient for modelling large clusters of spherical metallic NPs [30]. In particular, each nanosphere forming the necklace was modelled by a multipole (maximum order 5) placed at the centre of the sphere, similarly to the approach followed within the generalized Mie theory [31]. Additional multipoles (of order 3) were placed close to the gaps (at a distance of $2/3$ along the centre-surface axis) to fully capture the strong NP interaction. The calculations were carried out in air under plane wave illumination for different polarization configurations of the incident light. We simulate perfect regular hexagons formed by spherical Ag NPs with a diameter of 50 nm and separated by 2-nm gaps.

2.3 Optical characterization

The spatial distribution of the SHG was analyzed in confocal geometry by recording two-dimensional spatial maps for different polarization configurations of the fundamental beam. To that end a customized scanning confocal microscope (Olympus BX41) equipped with a two-axis XY motorized platform (0.3 μm spatial resolution) was used. A femtosecond Ti:sapphire laser (Spectra Physics Model 177-Series) tuned at 840 nm was used as a fundamental beam. This beam was focused on the sample surface by using a 100x microscope objective and the generated SHG signal was collected in backscattering geometry with the same objective. The SHG signal was detected with a Peltier cooled Hamamatsu R636 photomultiplier. The incident pump power was kept below 1 mW. The experimental extinction spectra were obtained in transmission geometry by using a double beam Lambda 1050 Perkin Elmer spectrophotometer.

3. Results and discussion

3.1 Plasmonic response of the hexagonal necklaces: far field and near field distribution

To gain a better understanding of the collective plasmonic modes associated with the hexagonal arrangements of interacting Ag NPs, we first evaluate the effect of the number of particles on the extinction cross section spectra. Figure 2(a) shows the simulated extinction spectra obtained for regular hexagonal necklaces with gradually increasing number of particles per side (N varying from 6 to 54 NPs). For the sake of comparison, the spectra were normalized to their maximum intensity. As seen, the spectra show a plasmonic resonance located at the near UV spectral region (350-370 nm) whose overall position is practically independent on the number of NPs forming the necklace. This resonance can be mainly associated with chain collective transverse modes sustained by the sides of the hexagons, which are spectrally located at similar spectral positions than that of isolated Ag NP and exhibit a cross-section value that increases linearly with the number of particles in the necklace side. A detailed inspection reveals the presence of two nearby peaks at around 350 and 370 nm, which have been previously assigned to a dipole (370 nm) and a quadrupole resonance (350 nm) of the nanoparticle chains [32].

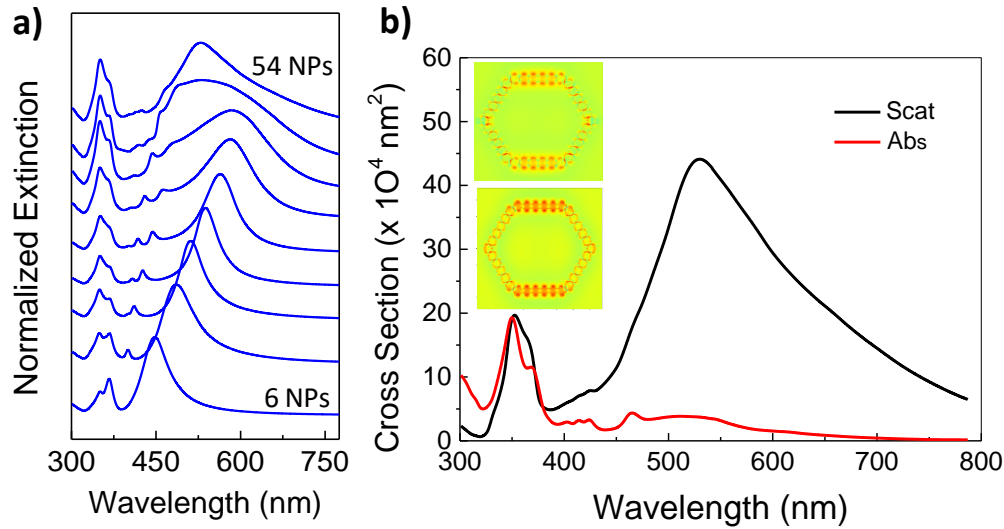


Fig. 2. a) Evolution of the normalized far field extinction spectra calculated for regular hexagonal necklaces of silver nanoparticles when the number of NP in the hexagon is increased from 6 to 54 NPs. The spectra have been vertically shifted for the sake of comparison. b) Absorption and scattering cross-section spectra of a hexagonal necklace containing 54 NPs. The insets show the calculated near-field patterns of the in-plane component normal to the horizontal side of the hexagon at 370 nm (upper panel) and 350 nm (bottom panel) obtained for a plane wave polarized perpendicular to the horizontal hexagon side and normal incidence.

As observed in Fig. 2(a) the spectra also exhibit an intense plasmonic resonance at lower energy, which is related to the longitudinal collective plasmon of the necklace. As the number of NPs in the necklaces is increased this resonance shifts to longer wavelengths until it stops red shifting at around 530 nm, which occurs for hexagons formed by 54-60 NPs (around 10 NPs per side). This low energy resonance also displays a noticeable broadening when increasing the number of particles due to the spectral overlap of several higher-order plasmon resonances lying in the visible region, which are also red-shifted. Those higher-order plasmon resonances are hybridized modes originating from the coupling of quadrupolar modes of the individual spheres, which for the case where not all dipoles in the chain are parallel, also appear at similar energies and further broaden the main peak in the spectra [32–35].

The overall behavior of the low energy mode is similar to the longitudinal collective mode observed in linear chains of interacting NPs. As reported, this mode redshifted and broadened as the number of particles was increased up to 10-15 NPs in which a saturation of its spectral position was observed [32–39]. Additionally, the radiative and non-radiative character of the plasmonic resonances is also analogous when comparing both systems, the necklace and the linear chain. Figure 2(b) displays the absorption and scattering cross-section spectra calculated for a large hexagon containing 54 NPs. The insets show the near-field patterns of the in-plane component normal to the horizontal side of the hexagon at 370 nm (upper panel) and 350 nm (bottom panel) obtained for a plane wave polarized normal to the hexagon side. As shown in the patterns, the absorption losses at 350 nm are clearly higher than those at 370 nm (notice the loss of perfect metal character at 350 nm on the horizontal side of the hexagon). The near field patterns illustrate the difference observed in the absorption spectra at those wavelengths.

On the other hand, while the plasmonic mode at high energy exhibits a noticeable absorption, the character of the lower energy mode is mainly radiative with scattering cross-section values one order of magnitude larger than the absorption ones. These results are analogous to those reported for linear chains [38] and indicate that the far field spectral

response is dominated by the collective radiative mode, which extends from the visible down to the near infrared region. The analogy with linear chains also helps to understand why the saturated spectra are blue-shifted compared to those of intermediate hexagons. For small hexagons, the mode shifts originate from the increasing number of NPs forming chains parallel to the incident polarization, but also from the interaction between parallel chains (top and bottom hexagon sides). For larger hexagons, the two sides are well separated and their interaction is minimal, so that only the single-chain modes contribute to the spectra.

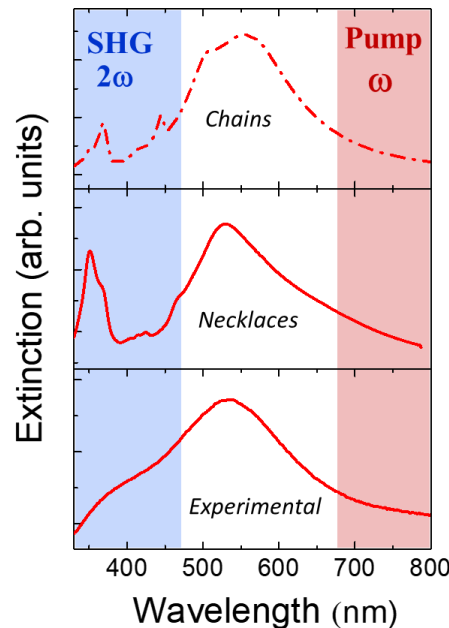


Fig. 3. Top panel: Calculated extinction cross section spectrum for a linear chain composed of 10 NPs for an electric field oscillating parallel to the chain. Central panel: Extinction cross-section spectrum calculated for a hexagonal necklace containing 54 NPs. Bottom panel: experimental extinction spectrum of the fabricated necklaces composed by several hundreds of NPs. The shaded regions in red and blue colors denote the spectral ranges associated with the fundamental and SHG regions involved in the frequency conversion processes.

Figure 3 shows the extinction cross-section spectrum calculated for a linear chain composed by 15 NPs together with that of a plasmonic hexagon formed by 54 NPs. These spectra are compared with the experimental one, which was obtained for an arrangement of non-interacting hexagons formed by several hundreds of NPs (See Fig. 1). As observed, they all show similar spectral features even if the total number of involved nanoparticles is different. This relatively good correlation indicates that the spectral response of the hexagonal arrangements formed by a large number of strongly interacting metallic NPs is governed by the longitudinal linear chain plasmon mode associated with each side of the arrangement. Additionally, the experimental result confirms the predicted calculated saturation position of the mode, as observed from the similar spectral position of the maxima in the three spectra. Figure 3 also illustrates the spectral regions of a fundamental beam and its corresponding SHG that could simultaneously match the plasmonic response of the hexagonal necklaces. In particular, a fundamental beam lying in the red shaded region would produce the excitation of the long-wavelength radiative mode, while the corresponding SHG signal would excite the plasmonic resonances lying in the UV-VIS spectral region (blue shaded region). We stress the presence of a spectral shoulder in the near UV region, which correspond to the high energy modes at around 350 nm in the numerically calculated spectrum. Here, let us recall that the experimental extinction spectrum of the necklaces was obtained in transmission geometry

after subtracting the contribution of the LiNbO_3 crystal. Hence, the accuracy of the experimental spectrum in the high energy region is limited, among others, by the increasing values of the optical density below 400 nm due to the absorption edge of the LiNbO_3 crystal, which prevent a precise resolution of the peaks at around 350 nm.

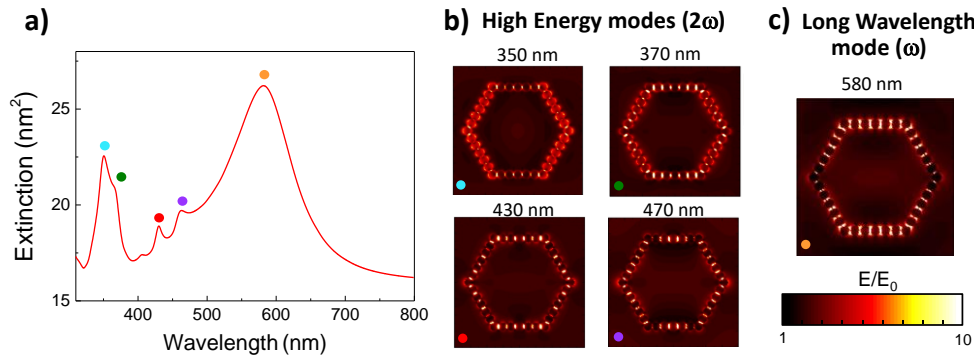


Fig. 4. a) Extinction cross section spectrum calculated for hexagons containing 6 NPs per side. b) Near field distributions of the high-energy modes. The upper panels correspond to the double peak structure located in the near UV spectral region (350 nm and 370 nm, respectively). The bottom panels refer to the higher-order resonances at the blue spectral regions. Namely, the spectral structure centered at around 425 nm and the side band peaking at around 470 nm. The colored dots indicate the spectral positions at which the near field distributions were computed. c) Near-field profile associated with the long-wavelength plasmonic mode centered at around 580 nm. At this wavelength, the maximum field enhancement at the gaps is around 100. The polarization of the incident light was parallel to the horizontal axis in all cases.

Further physical insight into the behavior of the plasmonic modes supported by the necklaces has been obtained by analyzing the near field distribution at the frequencies of the different resonant peaks in the far field spectra. The calculations were performed in air for a plane wave polarized parallel to the horizontal side of the hexagon (x axis). In this respect, we would like to note that though the maximum field enhancement value at the gaps between the particles is around 100, the plots were saturated at 10 to better show the distribution of the plasmonic mode. For illustrative purposes, Fig. 4 shows the results obtained for hexagons containing 6 NPs per side. There, the near field distributions of the plasmonic modes related to the relevant peaks in the corresponding cross-section spectrum [Fig. 4(a)] have been depicted. As observed in Fig. 4(b), the field enhancement of the short-wavelength modes at 350 nm is less than that of the low energy mode. This high energy mode is mainly excited around the individual nanoparticles of the sides which are not parallel to the polarization of the incident plane wave, as expected from its transverse character. On the other hand, the field intensity distribution computed at the blue spectral region (425 nm and 470 nm) displays a more complex profile due to the excitation of high-order plasmonic modes as well as to the merging of the chain like modes. The near field associated with the long-wavelength plasmonic resonance is also shown [Fig. 4(c)]. As seen, this mode is characterized by a large electric-field enhancement at the gaps between the NPs (in a factor of around 100). Additionally, it displays a spatial distribution similar to that reported for curved chains, being the effective plasmonic chain mode robustly preserved through the corners of the hexagon [35, 36]. At this point, we would like to note that even when the field enhancement reported here was obtained in the nanoparticle mid-plane, the obtained values are large enough to ensure that the field enhancement enters the substrate. Indeed, similar near field enhancements have been recently exploited in the design of plasmon assisted solid-state nanolasers [40, 41]. On the other hand, tuning the wavelength across the same plasmonic mode does not produce a relevant variation of the near field distribution, but significant

changes of the enhancement values. In our case, we have obtained the near field patterns at the maximum of each spectral resonance.

3.2 Polarization dependence of the plasmonic coupling

We have also studied the extinction spectra and the near field profiles associated with the long-wavelength plasmonic mode for different polarization configurations of the incident light. Figure 5(a) displays the near field distribution in the vicinities of the hexagonal necklaces for three different polarization configurations of the incident beam: parallel to the horizontal side of the hexagon ($\theta = 0^\circ$), perpendicular to it ($\theta = 90^\circ$) and at an intermediate angle ($\theta = 45^\circ$). The results show that the enhanced field distribution around the particles is strongly dependent on the polarization direction of the incoming field. More specifically, the intensity of the field in the gaps between the particles is maximum at those hexagon sides parallel to the input polarization, which again agrees well with behavior of the longitudinal mode sustained by linear chains. Indeed, rotating the input linear polarization results into a spatial redistribution of the maximum/minimum coupling strength along the different hexagon sides [see Fig. 5(a)].

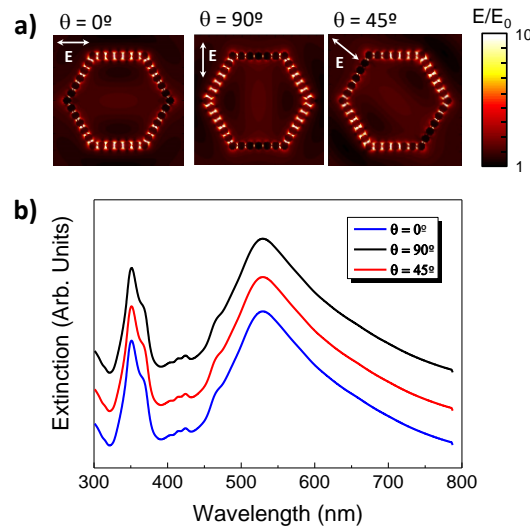


Fig. 5. a) Near field distribution associated with the dominant long-wavelength mode calculated for different polarization orientations of the incoming electric field: $\theta = 0^\circ$, 45° and 90° . The maximum field enhancement at the gaps is around 100. To better illustrate the details, the plots were saturated at $E/E_0 = 10$. b) Far field extinction cross-section spectra calculated for hexagons containing 54 NPs for three different polarization orientations of the incident plane wave. The spectra have been vertically shifted for the sake of clarity.

On the other hand, as depicted in Fig. 5(b), the cross section spectra of the hexagons is identical for the different orientations of the incoming electric field, i.e the optical features of the extinction spectrum remain unaffected regardless the polarization direction of the incident wave. This polarization insensitive behavior of the spectrum relies on the rotational symmetry of the hexagons (quasi-circular character) and it is consistent with the fact that the plasmonic mode is preserved through the corners in such a way that for every polarization the number of particles participating in the effective chain remains the same [see Fig. 5(a)]. The results are in agreement with previous works [42–44], and point out the potential of these high symmetry plasmonic arrangements for enhanced optical processes. In particular, these arrangements provide broadband plasmonic response to spectrally overlap the fundamental and SHG waves involved in a frequency conversion process without restrictions on the polarization direction of the incoming electric field. Moreover, the ability to manipulate the spatial distribution of

the field enhancement by rotating the input linear polarization without affecting the far-field spectral properties provides alternative pathways for a controlled directionality of the enhanced optical processes at the nanoscale.

3.3 SHG imaging experiments

To experimentally probe the optical response of the plasmonic hexagons and their near field features, we evaluate the SHG signal obtained at the immediacy of the metallic arrangements for different polarization configurations by using spatially resolved SHG microscopy. Figure 6(a) shows a representative SEM image of the scanned area. The SHG images were obtained by scanning the fundamental beam on the region of each hexagonal necklace, so that the influence of possible collective interactions between the hexagons can be disregarded. The fundamental wavelength was fixed at around 840 nm. At this wavelength there is still an appreciable spectral overlap between the long-wavelength resonance and the fundamental radiation. On the other side, the SHG at twice the energy of the fundamental beam (420 nm), is resonant with the spectral shoulder in the blue spectral region of the extinction spectrum.

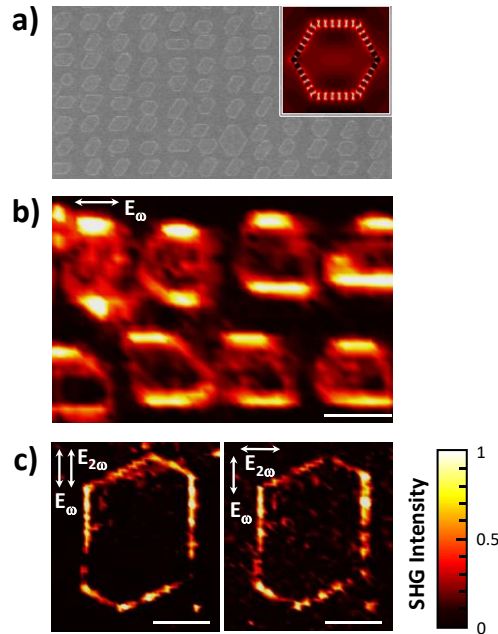


Fig. 6. a) Representative SEM image showing several plasmonic necklaces organized on the polar surface of a LiNbO_3 crystal. The inset displays the near field distribution of a single hexagon computed for the collective long-wavelength plasmonic mode when the incoming electric field was linearly polarized along one of the hexagon sides, $\theta = 0^\circ$. b) SHG intensity map recorded for a fundamental beam polarized parallel to a hexagon side ($\theta_{\text{pump}} = 0^\circ$). c) Spatial distribution of the SHG intensity analyzed at $\theta_{\text{SHG}} = 0^\circ$ and $\theta_{\text{SHG}} = 90^\circ$. In both cases, the polarization angle of the fundamental beam was $\theta_{\text{pump}} = 0^\circ$. The scale bar in panel b) and c) is equal to 5 μm .

Figure 6(b), displays the unpolarized SHG intensity map obtained for a fundamental beam linearly polarized with the electric field parallel to one of the hexagon sides ($\theta_{\text{pump}} = 0^\circ$). In Fig. 6(c), we maintain the polarization of the pump beam at $\theta_{\text{pump}} = 0^\circ$ (parallel to one of the hexagon side) and analyze the polarization of the SHG signal at orthogonal angles $\theta_{\text{SHG}} = 0^\circ$ and $\theta_{\text{SHG}} = 90^\circ$. For both configurations, the SHG signal collected at the immediacy of the metallic arrangements was notably enhanced with respect to that obtained from the bare LiNbO_3 crystal showing maximum enhancement values of around 10. The SHG intensity profile depends on the hexagon side, being more intense from those sides parallel to the

polarization of the fundamental beam. Indeed, we notice the good correlation between the spatial distribution of the enhanced SHG and the calculated near field enhancement of the long wavelength mode when the electric field is polarized parallel to the hexagon sides [see inset in Fig. 6(a)]. Additionally, the results also shows that the SHG distribution intensity does not exhibit significant changes when analyzing the SHG polarization for $\theta_{\text{SHG}} = 0^\circ$ and $\theta_{\text{SHG}} = 90^\circ$ [Fig. 6(c)]. Therefore, we can conclude that the enhanced SHG signal is mainly governed by the field enhancement of the fundamental beam mediated by the long-wavelength plasmonic mode. This long wavelength mode spectrally overlaps the fundamental beam and it is responsible for the near field enhancement of the fundamental radiation and therefore of the generated SH signal. In this sense, even though some nonlinear contribution of the metallic nanoparticles to the overall SHG signal cannot be fully disregarded, our results can be explained by taking into account the linear response of the necklaces, according to our experimental and theoretical results. Indeed, the results are consistent with the two-photon character of the nonlinear process, which involves a quadratic dependence on the near field enhancement of the pump wavelength.

4. Summary and conclusions

To summarize, we have studied the influence of the polarization and wavelength on the plasmonic response of hexagonal necklaces prepared by a very simple and cost-effective photo-reduction method.

On the one hand, we have shown that the far-field spectral response of large metallic closely resembles that encountered in circular assemblies in which the far field extinction response remains invariant with the polarization state of the incoming light. Further, by rotating the incoming linear polarization we show the possibility to control the spatial distribution of the near-field enhancement sustained by the necklaces without affecting the far field properties, which is of interest in applications involving the interaction of optical fields at different spatial regions.

On the other hand, the potential of hexagonal necklaces for plasmon-enhanced optical processes was further validated through the analysis of the SHG spatial distribution obtained for different polarization configurations of the involved optical fields. By using spatially resolved SHG microscopy we found that the near field components associated with the low energy mode govern the spatial distribution of the enhanced SHG. Hence, it was possible to identify the dominant mechanism of the SHG enhancement even though we were involving the excitation of a set of plasmonic resonances that simultaneously match the pump and the SHG signal (multimode matching). The results evidence the potential of hexagonal necklaces of interacting NPs as useful platforms for SHG enhancement at the nanoscale in a broad spectral range.

Funding

Spanish Ministry of Economy and Competitiveness (MINECO) under project MAT2016-76106-R and the Comunidad de Madrid (grant S2013/MIT-2740). C.T. acknowledges funding from the VILLUM Foundation (Villum Investigator, grant no. 16498). L.E.B and M.O.R also acknowledges financial support from the Spanish Ministry of Economy and Competitiveness, through The “María de Maeztu” Programme for Units of Excellence in R&D (MDM-2014-0377). ”.